17 May 2023

Effect of Cr and Ni Concentrations on Resilience of Cast Nb-Alloyed Heat Resistant Austenitic Steels at Extreme High Temperatures

Simon N. Lekakh
Missouri University of Science and Technology, lekakhs@mst.edu

Mario F. Buchely
Missouri University of Science and Technology, buchelym@mst.edu

Mei Li

Larry Godlewski

Recommended Citation

S. N. Lekakh et al., "Effect of Cr and Ni Concentrations on Resilience of Cast Nb-Alloyed Heat Resistant Austenitic Steels at Extreme High Temperatures," *Materials Science and Engineering A*, vol. 873, article no. 145027, Elsevier, May 2023.
The definitive version is available at https://doi.org/10.1016/j.msea.2023.145027

Materials Science & Engineering A 873 (2023) 145027

Contents lists available at ScienceDirect

Materials Science & Engineering A

journal homepage: www.elsevier.com/locate/msea

Effect of *Cr* and *Ni* concentrations on resilience of cast *Nb*-alloyed heat resistant austenitic steels at extreme high temperatures

Simon N. Lekakh [a,*], Mario Buchely [a], Mei Li [b], Larry Godlewski [b]

[a] Missouri University of Science and Technology, Rolla, MO, 65409, USA
[b] Research and Innovation Center, Ford Motor Company, Dearborn, MI, 48124, USA

ARTICLE INFO

Keywords:
Heat resistant austenitic steel
Oxidation
Thermal cycling

ABSTRACT

Austenitic *Cr–Ni* alloyed heat resistant steels with *Nb* additions are used for intensively thermo-mechanically loaded cast components working in extreme high temperature oxidizing environment. Their performance during static oxidation and transient thermo-mechanical loading was investigated to recommend an optimal cost-effective *Cr/Ni* composition of *Nb*-alloyed austenitic class steels. The static oxidation and transient thermo-mechanical behavior of three austenitic steels with different *Cr/Ni* alloying levels were investigated and compared for variety of working conditions. Static oxidation was performed between 900 °C and 1000 °C in air for 400 h. The critical temperature which increases spallation during static oxidation was determined for each of the steel alloying levels. In addition, thermal cycling of a constrained specimen was done with varying upper cycling temperatures between 850 °C and 1000 °C. SEM and TEM analyses were supported by thermodynamic simulation of the phases precipitated in the metal matrix and the structure of formed oxide layers. These studies were used to determine the mechanisms of degradation of thermo-mechanically loaded *Cr/Ni* austenitic steels at extreme high temperatures. A recommendation for a cost-effective *Cr/Ni* alloying level for different working conditions was determined.

1. Introduction

There are a variety of cast components produced from heat resistant *Cr/Ni* austenitic steels, including turbochargers, furnace fixtures and large castings used for power and chemical industries. These castings need to resist degradation during life-time service in severe conditions when subjected to thermo-mechanical load and high temperature oxidation. These components are produced accordingly to ASTM standards, such as A447, A890, and A297 *Fe–Cr–Ni* heat resistant castings for general applications, A744 for severe service, and for specific parts: working under pressure - A351, heavy-walled castings for steam turbine - A356, investment casting – A957, and A608 for centrifugally cast [1]. Conventional *Cr–Ni* austenitic heat resistant cast steels are used to make components for mild and moderate severity of thermal oxidation and different *Cr/Ni* levels are recommended depending on the maximum service temperature [2]. It is generally known that increasing *Cr* and *Ni* is an effective way to improve heat resistance [3]; however, these alloying elements are relatively expensive, and significant additions could not be the preferred choice for improving high-temperature mechanical properties from the viewpoint of production cost. Also, *Ni* is not effective for improving high-temperature creep resistance.

The addition of alloying elements, such as *Nb*, *Ti* and *Mo* instead of increasing *Ni* were used in different compositions of heat and creep resistant austenitic steels. As compared to other alloying elements, it was proven that *Nb* is very effective to increase high temperature creep resistance [4]. The effect of *Nb* on the microstructure and thermal-shock resistance was investigated for as-cast and annealed JIS SCH21 steels [5]. Primary *NbC* carbides were crystallized together with $M_{23}C_6$ at the grain boundary of a as-cast steel. It was found that chromium carbides had low thermal stability; however, the primary *NbC* carbides played a significant role in preventing the propagation of micro-cracks and restraining the component shape deformation when exposed to heating and quenching. The addition of *Nb* in a conventional heat resistant steel promotes changes in the microstructure which enhance the reduction of the number and average length of cracks when exposed to continuous heating/cooling cycles in non-protected atmosphere [6]. The authors studied the morphology of *Nb* carbonitrides which precipitated in the austenitic steel and its effect on the creep behavior [7] and thermo-mechanical fatigue [8,9]. The oxidation behavior at 900 °C in air using a 22% *Cr* and 25% *Ni* austenitic alloy was improved when 0.86% *Nb* was

* Corresponding author.
E-mail address: lekakhs@mst.edu (S.N. Lekakh).

https://doi.org/10.1016/j.msea.2023.145027
Received 20 March 2023; Received in revised form 5 April 2023; Accepted 6 April 2023
Available online 14 April 2023

added due to a change in the oxide scale structure [10]. The role of *Nb* in austenitic steels was summarized in Ref. [11].

Therefore, austenitic *Cr–Ni* alloyed heat resistant steels with *Nb* additions are promising for cast components which are targeted for intensively thermo-mechanically loaded along with exposure to high temperature oxidation conditions. Due to external surface degradation and variations within the micro-structure, the optimal *Cr/Ni* alloying level in *Nb*-bearing austenitic steels will depend on temperature, atmosphere, and thermo-mechanical loading parameters. Therefore, increasing only the *Cr/Ni* levels may not simultaneously improve both static oxidation resistance and transient thermo-mechanical behavior.

In our previous publication [12], three *Nb*-bearing steel compositions with variations in *Cr/Ni* concentrations were cast and used to study static oxidation. These compositions were also used in this study with the goal of the experimental verification of static and transient thermo-mechanical behavior and to determine a cost-effective *Cr/Ni* concentration for different severity of high temperature service.

2. Materials and methods

2.1. Studied steels

Three *Nb*-bearing heat resistant *Cr–Ni* austenitic steel with different *Cr/Ni* concentrations (20/10, 22/11 and 26/16) were studied. These steels had additions of *N* and *Mn* to stabilize the austenite and *Si* to improve the oxidation resistance (Table 1). More details about these steels can be found in previous article [12]. For simplicity in this article, the steels will be referred as following: (A) economical, (B) medium alloyed, and (C) high alloyed by *Cr/Ni*. Similar grades are common for castings working in harsh environments. To verify that the steels were within the austenitic range, compositions were plotted in the Schaeffler *Cr/Ni* equivalent phase diagram, as shown in Fig. 1, where the red dots indicate the three studied materials. The steels were produced by melting the calculated raw materials in a 100 kg capacity induction furnace under *Ar*-gas flow protective atmosphere. Liquid metal was poured into the no-bake sand molds to produce casting of 18 mm wall thickness vertical plates with top riser.

Thermodynamic simulations of the sequences of phase formations during melt cooling and in solid state condition in the studied class of steel were obtained from FACTSAGE thermodynamic equilibrium simulations and shown in Fig. 2 for steel B. To illustrate the phase formation sequence from liquid to solid during solidification, an inverse temperature was used (decreasing from left to right). Solidification in all three alloys started as austenite and *Nb*-carbonitrides precipitates directly from the liquid near the end of solidification. In the solid-state condition, the *Cr–Fe* carbide solution precipitated below 1100 °C and additionally, the *Z*-phase and Sigma phase can also be formed in the solid-state reactions according to equilibrium.

The SEM/EDX analysis of Steel B (Fig. 3) supports thermodynamic prediction of the solidification sequence: *Nb*-carbonitrides decorated the boundaries of primary austenite dendrites because they were directly formed from the melt at the end of solidification. In studied alloys, the *Nb*-carbonitrides (2 in Fig. 3) had a lamella shape and were dispersed at the austenite (1) boundaries. Observation under higher magnification showed signs of solid state formed *Cr–Fr* carbides (3) along the inter-dendritic region. The other predicted equilibrium phases (Fig. 2) were not present in as-cast condition, thus indicating a possible austenite supersaturation during casting cooling. Detailed higher resolution TEM study was performed for high temperature tested steels to determine the other possible equilibrium precipitates predicted from thermodynamic simulation.

Table 1
Composition of studied austenitic steel (wt. %).

Steel	*C*	*Si*	*Mn*	*Cr*	*Ni*	*Nb*	*N*
A	0.3	1.5	1.0	**20**	**10**	2.0	0.2
B	0.41	1.6	1.8	**22**	**11**	1.5	0.1
C	0.41	1.2	1.9	**26**	**13**	1.7	0.1

2.2. Static oxidation tests

The procedure for static oxidation was presented in our article [12] and the obtained data will be discussed in this article in conjunction with the new results from the transient thermo-mechanical tests. In summary, rectangular 35 × 15 × 5 mm samples for oxidation were machined from plate castings with wet grinding using 60 grit silicon carbide. Static oxidation testing was performed in still air at 900 °C, 950 °C and 1000 °C for a duration of 400 h. Cylindrical alumina crucibles with the specimen inside were used to collect the spalled scale and to measure the weight change of the specimen with adherent oxide layer. The oxygen mass percentage in the spalled scale was evaluated using LECO *N/O* analyzer. This data, along with the observed geometry of spallation spots were used to determine the time-dependent process of spallation assisted oxidation. The details of simulation of spallation assisted oxidation kinetics using the stochastic simulation model were described in a previous work [13]. Briefly, the stochastic model considers the topology of spalled scale and spallation intensity which allows the determination of the real oxidation kinetics which formed the adherent oxides and the scale spallation kinetics. The determined from experiment and simulation an amount of oxygen (mg/cm^2) within the adherent oxide layer and in the spalled scale were used for characterization of the static oxidation rates.

XRD analysis of oxidized surface showed a mixture of iron and chromium oxides (Fig. 4a). FACTSAGE thermodynamic simulations can predict multilayered scale structures, consisting of external *Fe*-oxides, internal *Cr–Fe* oxide mixture, and pure *Cr*-oxide sublayer which are strongly adherent to the matrix (Fig. 4b). Therefore, when cracking and spallation occurs at the boundary between these layers, the spalled scale topology can be defined from experimental observation of the oxidized surface using a *Cr* surface map (Fig. 4c and d) and Table 2.

2.3. High temperature physical properties

Thermal diffusivity and thermal conductivity are the important physical properties for materials used at transient temperature cycling conditions; therefore, the laser flash (LF) method was used to quantify thermal diffusivity. To obtain reliable data, all alloys were tested simultaneously. The values of the coefficient of thermal conductivity were determined from the experimental value of thermal diffusivity and tabulated values of density and specific heat capacity obtained from JMatPro software.

2.4. Tensile test

Tensile tests were performed using a MTS load frame equipped with high-temperature furnace and external LVDT type extensometer. Room and high temperature (from 800 °C to 1000 °C) tensile tests were performed using three material conditions: (i) specimens machined from as-cast plate, (ii) specimens machined from the body of annealed bars at 1000 °C during 400 h (removing oxide scale from surface), and (iii) machined tensile specimens with oxidized surface after annealing in air at 1000 °C during 400 h. Test (ii) was perform to obtain the effect of possible structure transformations during high temperature annealing, which were predicted from equilibrium (Fig. 2), whereas the test (iii) was performed to evaluate the possible effect of surface degradation due to oxidation.

2.5. Thermal cycling test

In addition to being exposed to harsh high temperature oxidizing environments, cast components from austenitic steels are often

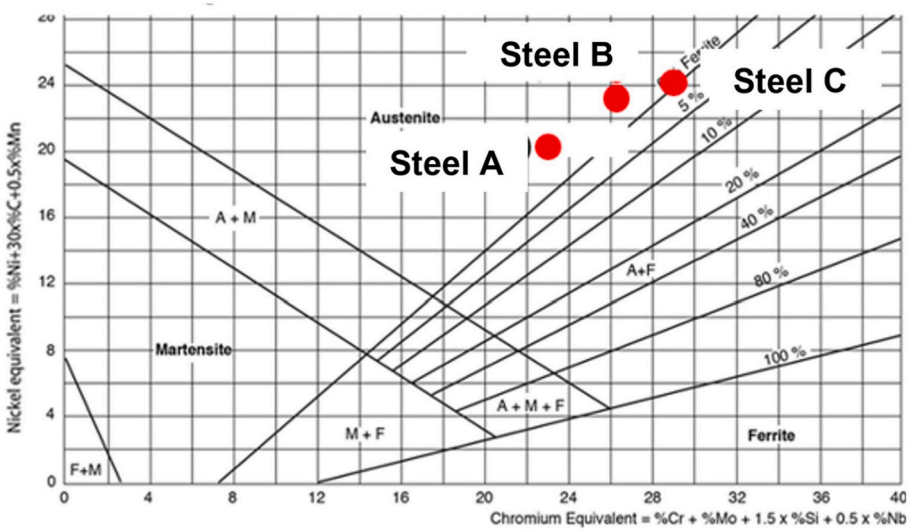

Fig. 1. Schaeffler *Cr/Ni* equivalent diagram, including the three studied steels (red dots). (For interpretation of the references to colour in this figure legend, the reader is referred to the Web version of this article.)

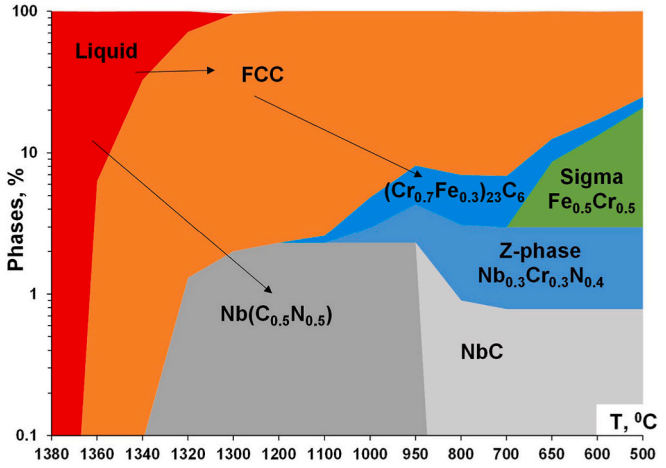

Fig. 2. Calculated with FACTSAGE sequence of solid phase formation during solidification and casting cooling in steel B (from left to right) under equilibrium conditions.

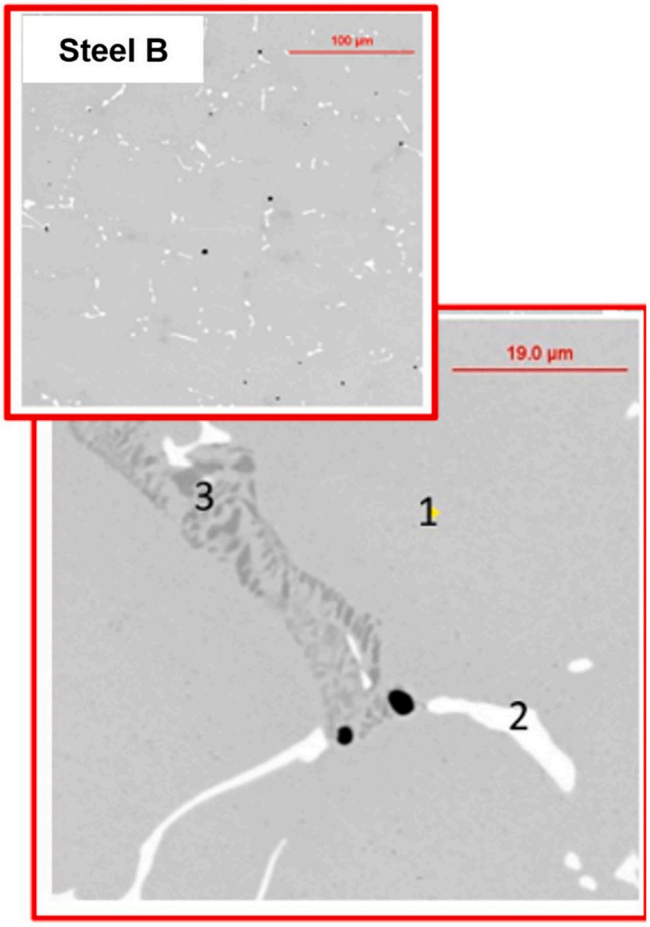

Fig. 3. SEM observed microstructure of steel B at lower (top) and higher (bottom) magnifications: 1 – austenite, 2 – *Nb*-carbonitrides, and 3 – *Cr–Fe* complex carbides.

subjected to thermo-mechanical load during thermal cycling at mechanically constrained conditions. When these types of loads occur, the self-induced stress and strain will depend on both intrinsic (thermal expansion, heat conductivity and mechanical properties of material) and extrinsic (thermal load, component geometry) conditions. Joint effects of surface oxidation, near-surface thermal fatigue, and internal creep will determine the cast component performance in such harsh transient loading conditions. Therefore, joint evaluation of the high temperature performance of an austenitic steel during static oxidation as well as in transient thermo-mechanical loading conditions assisted by oxidation was done in this study to determine cost effective steel compositions for different working environment.

To experimentally replicate the behavior of mechanically constrained complicated shape cast component during transient thermal conditions, the thermo-cycling tests were performed using a custom Joule heating computer-controlled device, referred to the "Thermal Simulator", along with a specially designed specimen shape [14]. This specimen shape (Fig. 5) mimics changes in stress/strain triaxiality during thermal cycling which experience the real complicated shape cast components, for example cast manifold, due to thermal expansion while in a mechanically constrained condition. In previous study [14], this test was simulated using FEM and identified a high probably of crack formation at the internal corner area. The predicted location of crack formation was used to analyze micro-structure near crack tip. To study joint

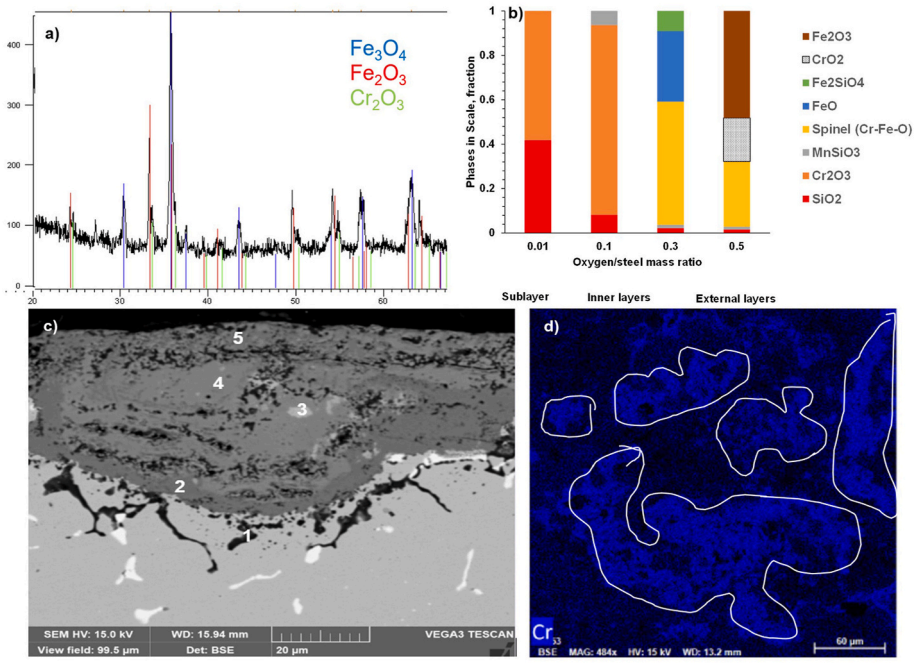

Fig. 4. XDR analysis of oxidized surface (a), thermodynamic predictions of multilayered scale structure (b), cross-section SEM image with points for EDX analysis (c), and *Cr* map from top view (d) of steel A oxidized at 1000 °C during 400 h. Spalled spots were outlined from *Cr*-map.

Table 2
EDX analysis of scale (wt. %) in steel A oxidized at 1000 °C during 400 h (points from Fig. 4c).

Point	O	Si	Cr	Mn	Fe	Ni	Nb
1	45	32	15	4	3	–	–
2	32	–	65	–	1	1	–
3	21	–	44	–	–	–	31
4	25	–	25	–	27	21	–
5	29	–	48	–	19	5	–

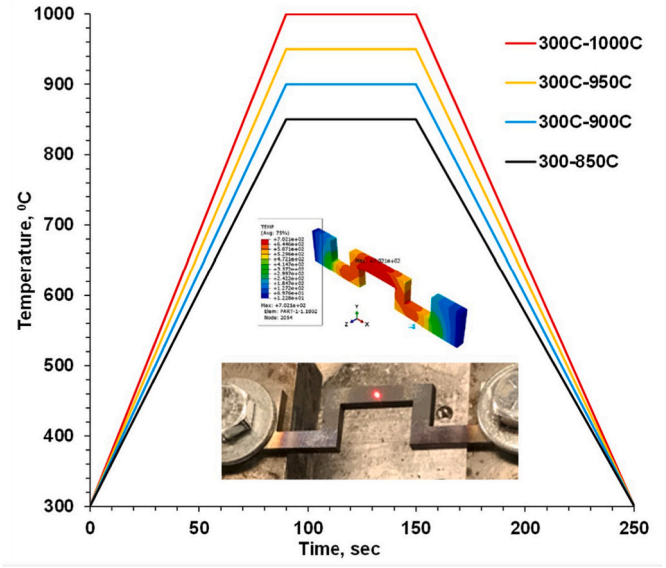

Fig. 5. Temperature - time (thermal) cycle schedules, tested and FEM simulated specimen (inserted figure).

effect of oxidation and self-induced thermo-mechanical load on crack formation during thermal cycling, four temperature/time schedules were used with variations in the upper holding temperature from 850 °C to 1000 °C with a constant 300 °C minimum temperature (Fig. 3). A zero force was set up prior to starting the test at 300 °C to compensate linear expansion when heating from room temperature. At several initial cycles, thermal expansion induced elastic compression force at high temperature. However, when the test continued, creep and plastic deformation in the hot zone changed the measured force to tension during cooling of the mechanically constrained specimen. Such changes in stress triaxiality are typical for many practical cases, for example in mechanically constrained exhaust manifold, the induced tensile strain can promote crack initiation during the cooling cycle. Details of the shape of generated tensile/compression forces hysteresis during initial and relaxation cycles were described in Ref. [14]. In this study, the developed tensile force at the end of each cycle was used to monitor crack initiation and 10% reduction in a maximal force was used as threshold to report number of cycles for crack propagation.

Transient thermo-mechanical load during thermal cycling of fully or partially constrained component is a typical type of load for many practical applications of cast heat resistant austenitic steel, for example, an exhaust system containing a turbocharger. The resilience of the cast component in such harsh environment depends on a combination of several material properties, including oxidation resistance, thermal conductivity, and mechanical properties, such as creep, fatigue, strength and ductility in wide range of temperatures. To analyze the effect of *Cr*/*Ni* concentrations on resilience of *Nb*-bearing austenitic steels at extreme high temperature, the standard test methods together with the specially designed testing methods were applied.

2.6. Structure analysis

SEM/EDX (Vega 3, Tecscan with Bruker spectrometer) analysis was performed on as oxidized surfaces to estimate spallation geometry and to evaluate the cross section of the scale structure and crack tip. The specimens for TEM analysis were prepared using focused ion beam (FIB) on a Thermo Fisher Helios 650 Nanolab SEM/FIB. The Scanning TEM (STEM) imaging was carried out using a Thermo Fisher Talos F200X

STEM operated at 200 kV and equipped with an integrated energy dispersive X-ray spectrometer (EDS) with four silicon drift detectors.

3. Results

3.1. Static oxidation

The static oxidation tests showed that a normal diffusion-controlled oxidation, which is characterized by parabolic decay of scale growth, rapidly accelerated due to scale spallation above a critical temperature. This critical temperature depended on steel *Cr/Ni* concentrations in *Nb*-bearing austenitic steel. The complexity of analyzing the experimental data for static oxidation above this critical temperature is illustrated in Fig. 6, using an example of oxidation kinetics for economical steel A with 20/10 *Cr/Ni* concentrations. These tests were performed between 900 °C, which is near the upper boundary, and to 1000 °C, which is above a critical temperature for this steel. In such severe conditions, the scale spallation significantly intensified the overall oxidation reaction rate. Raising the test temperature above 950 °C, significantly increased the total weight gain of the specimen and the weight of collected spalled scale (Fig. 6a). A significant amount of scale spallation occurred when test was performed at 1000 °C (Fig. 6c), while the actual weight of specimen with adherent oxide layer decreased (Fig. 6b). This happened because the spalled scale weight includes the weight of reacted oxygen and the weight of metal components transported from the steel into spalled scale. In such conditions, the data obtained from descaled specimens will not be enough to describe the kinetics of both processes.

Therefore, a special simulation/experimental procedure was implemented to decouple these two processes [13]. Calculated oxidation kinetics in the economical steel A, as shown below (Fig. 7a), for the critical temperature (Fig. 7b), and above the critical temperature (Fig. 7c) are shown using the same Y-scale on both graphs (a) and (b) and larger scale in graph (c) for visual comparison. At 900 °C, there is close to normal oxidation regime when forming an adherent oxide layer growing accordingly to the parabolic law which results in a limited formation of spalled scale. However, with increasing temperature to near critical, both, the forming adherent layer and the amount of spalled scale dramatically increase. At extreme high temperature, which is 1000 °C for this steel, the spallation dominated and practically all the formed oxides were immediately detached from the steel surface. In this regime, the total oxidation rate increased in order of magnitude with time because the austenitic steel lost the *Cr*-containing oxide film protection.

Fig. 8 compares oxidation of the three studied steels after 400 h holding time at 1000 °C. It is clear, that increasing the *Cr/Ni* concentration from 20/10 (A) to 22/11 (B) and 26/13 (C) *Nb*-bearing austenitic steels cardinally changed oxidation mechanisms. There is intensive spallation in the economical steel A, while there is a normal oxidation with forming a protection adherent oxide layer in high alloyed steel C. The medium alloyed steel B showed mixed oxidation kinetics at this temperature. These test results will be used to discuss the effect of *Cr/Ni* concentration in *Nb*-bearing austenitic steels on the critical temperature which occurs when diffusion-controlled oxidation mechanisms switched to spallation assisted oxidation.

3.2. High temperature physical properties

Fig. 9a illustrates the effect of temperature on experimentally measured thermal diffusivity of three studies steel using the LF method and Fig. 9b showed the calculated coefficients of thermal conductivity using the density and specific heat capacity values obtained from JMatPro software. Both, steady-state and transient heat conduction improved with increasing temperature, which is typical for the most austenitic steels, when compared to the other *Fe*-based alloys where heat conduction typically decreases at higher temperatures. There was not a significant difference between the thermal conduction in the studied steels, while the higher alloying level (steel C) provided a slightly higher conduction above 800 °C, which could potentially decrease self-induced strain during thermal cycling.

3.3. High temperature mechanical properties

Fig. 10 shows a summary of ultimate tensile strength (UTS) and elongation of the studied steels with as-cast structure at high temperatures. The goal of this test was the determination of steel softening which can occur at high temperatures, typically above 700 °C–800 °C for austenitic steels. Steel A showed higher UTS and lower elongation at 800 °C, while the intensive softening was observed with increasing test temperature. High alloyed by *Cr/Ni* steel C demonstrated higher tensile strength stability while the temperature increased and less softening. Steel B holds an intermediate position between these two steels. These results supported the well anticipated opinion that increasing *Cr/Ni* alloying level provided higher high temperature near-static mechanical stability.

3.4. Stability of mechanical properties after high temperature exposure

Fig. 11 shows a summary of ultimate tensile strength (UTS) and elongation of the as-cast and annealed steels with different surface quality (machined vs oxidized) at room temperature. As explained before, three conditions were examined: machined test specimens from as-cast plate, machined from annealed plate in air (1000 °C @ 4hr) plate to remove oxidized layer before test, and annealed of machined samples, which were tested with oxidized surface for determination of surface oxidation effect. All studied steels showed significant degradation of tensile strength and elongation after annealing when compared to as-cast condition. This was the result of precipitations and coagulation of dispersed phases from supersaturated austenite, mainly of which contained *Cr*-carbides, as observed in SEM inspection (Fig. 12). Additional surface oxidation of annealed specimens mostly affects elongation to failure while room temperature tensile strength degeneration not more than 20%.

3.5. Transient thermo-mechanical behavior

As explained before, these tests were performed on the custom-made Thermal simulator with self-induced force triaxiality fluctuation by changing compression/tension during the thermal cycling of special designed constrained specimen. Self-induced forces were collected during the test and data was processed to extract maximal tensile force

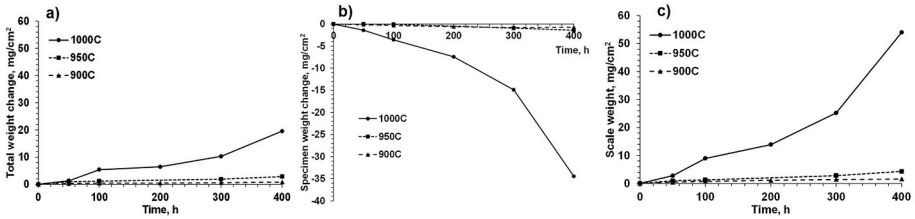

Fig. 6. Example of static oxidation test results of steel A by periodically monitoring weight: (a) total, (b) specimen, and (c) spalled scale.

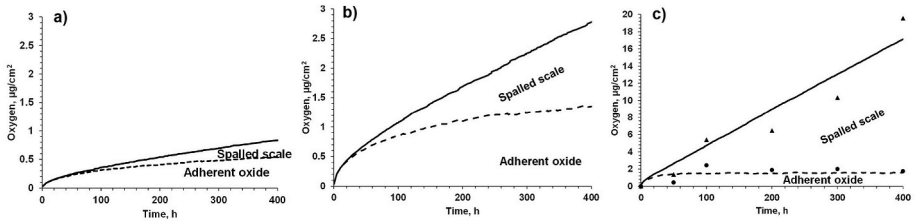

Fig. 7. Calculated/experimental kinetics of forming adherent oxide layer and spalled scale in steel A at 900 °C (a), 950 °C (b), and 1000 °C (c).

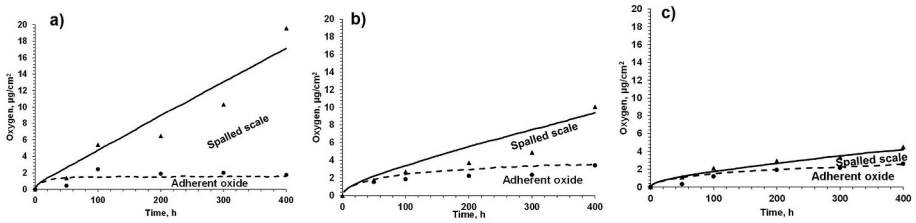

Fig. 8. Calculated (lines) and experimental (markers) kinetics of forming adherent oxide layer and spalled scale in steels: (a) A, (b) B, and (c) C at 1000 °C.

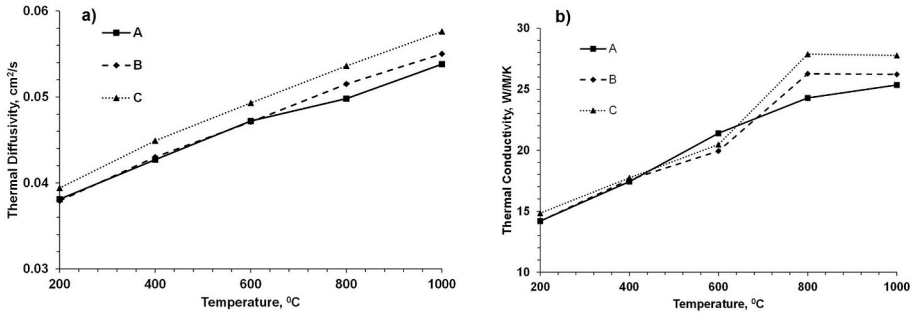

Fig. 9. Experimentally measured thermal diffusivity (a) and calculated thermal conductivity (b) of studied steels.

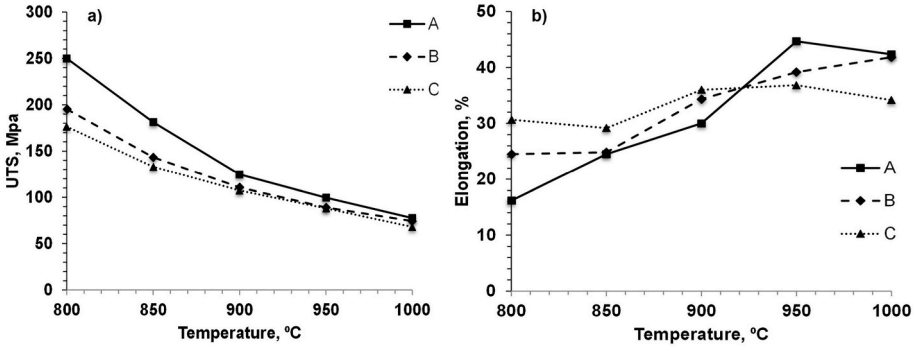

Fig. 10. High-temperature tensile properties of studied steels: (a) UTS, and (b) elongation.

at each cycle. This tensile force was a good indicator of crack formation and growth because the specimen degradation decreases it ability to develop tensile force in the constrained condition. Fig. 13 demonstrates changing the relative to maximum tensile force during cooling with increasing a cycle number for variety of upper temperatures, from near critical (850 °C) to extremely high (1000 °C) for economical *Nb*-bearing austenitic steel A with 20/10 *Cr/Ni* concentrations. At 850 °C, a small crack nucleated after ~500–800 cycles in the internal corner and continued to grow at a slow rate as the cycles increased up to 2100 cycles (Fig. 14a). The crack tip propagated through interdendritic network jumping from oxidized *Cr/Fe* carbide to partially oxidized *Nb* carbonitrides (Table 3). It is apparent that during this testing temperature/time combination, the crack tip formed first and oxidation within the open crack surface followed during this process. The failure sequence changes when the upper cycling temperature increased above a critical oxidation temperature for this alloy, which was around 900 °C. Fig. 14b demonstrates pre-oxidized layer in front of the crack tip at 950 °C upper test temperature. The crack growth rate dramatically increased at 1000 °C upper test temperature and resulted in an abrupt failure after ~750 cycles. While being exposed to such extreme temperatures, the failure mechanism changed again to transgranular propagation of the crack with multiple tips moving through the severely oxidized subsurface regions.

Thermo-cycling behavior of high alloyed steel C with 26/13 *Cr/Ni*

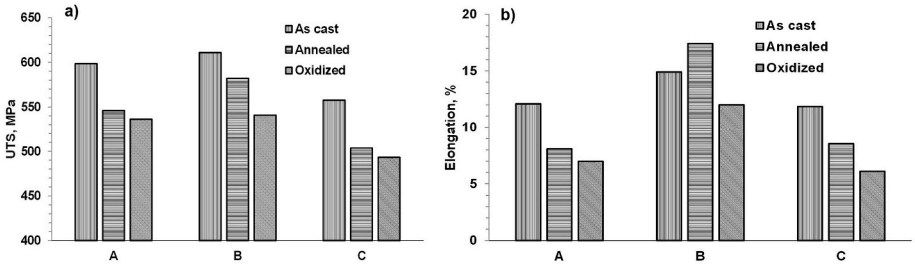

Fig. 11. Room temperature tensile properties comparison between three examined conditions: as cast, after annealing, and annealed with surface oxidation of studied steels (A, B, and C): (a) UTS, and (b) elongation.

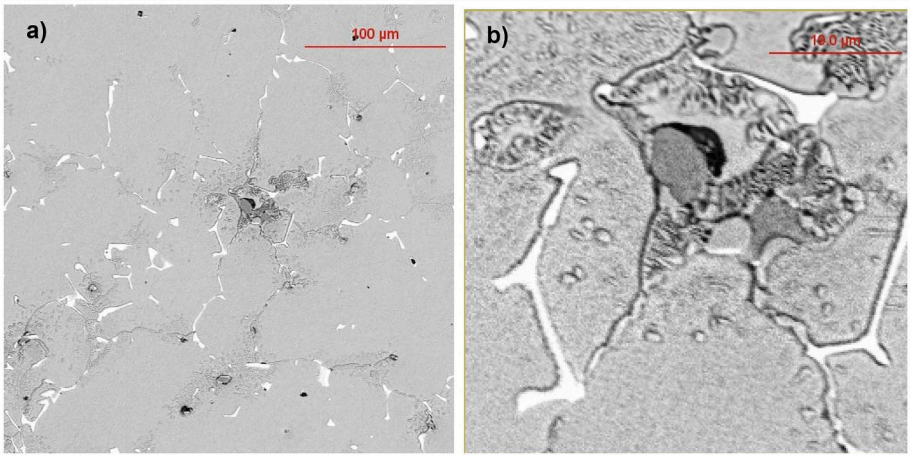

Fig. 12. SEM analysis of annealed steel A at different magnifications which illustrated grain boundary precipitates (a) and dispersed phases in the matrix (b).

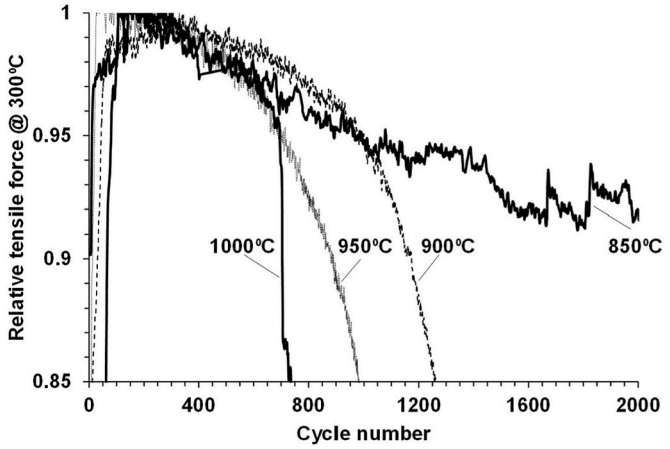

Fig. 13. Thermocycling curves of steel A when applying different upper temperatures.

concentrations was significantly different (Fig. 15) when compared to economical steel A with 20/10 *Cr/Ni* concentration. There was no period of slow rate of crack propagation with slow slope on tensile force vs cycle number at 300–850 °C as exhibited in Steel A. Instead, the tensile force initially increased indicating the strengthening due to formation of fine precipitation and after that was parabolic decline in the tensile force. The other difference was during testing at 300–1000 °C, the high alloyed steel C withstood a significant higher number of cycles before failure as compared to steel A. Actually, increasing the upper test temperature from 900 °C to 1000 °C had minor effect on the critical cycle number in steel C. At upper test temperature 900 °C, the tip of crack did not have a significant oxide layer and the crack propagated through the grain boundary network with sharp change direction (Fig. 16a) indicating a brittle failure mechanism. At upper test temperature 1000 °C, the radius of crack tip increased with the presence of the scale along crack path.

The medium alloyed steel B with 22/11 *Cr/Ni* concentration, exhibited an intermediate behavior between the economical steel A and the high alloyed steel C. Fig. 17 illustrates the partially oxidized crack tip after 1830 cycles tested at 300–900 °C, and heavy oxidized surface after 1089 cycles at 300–1000 °C.

4. Discussion

Experimental data provided an actual weight of oxygen in the adherent oxide and the spalled scale which along with stochastic simulations were used to decouple the kinetics of the actual oxidation with the forming the adherent oxide layer and the intensity of scale spallation in the three *Nb*-bearing austenitic steels with a variation in *Cr/Ni* alloying levels at different temperatures. This study revealed different types of the overall oxidation kinetics (Fig. 18). The first type of kinetics, in the case of limited spallation with almost adherent scale to the specimen surface follows the parabolic law (Fig. 18a). In another more extreme case (Fig. 18b), when a large spallation intensity takes place, there is a short initial period of adherent scale growth followed by an intensive scale spallation which removes all newly formed oxides from the interface, leaving only a tiny adherent layer. There also is a variety of intermediate spallation assisted oxidation kinetics which also were observed in this study (Figs. 6–8).

The summary of experimental tests for steady state oxidation at 400 h in air are presented in Fig. 19. The experimental results showed that the static oxidation resistance improves with increasing *Cr/Ni* ratio for the economical steel A (20/10), to the medium alloyed steel B (22/11) and finally, to the high alloyed steel C with 26/13 *Cr/Ni* concentrations.

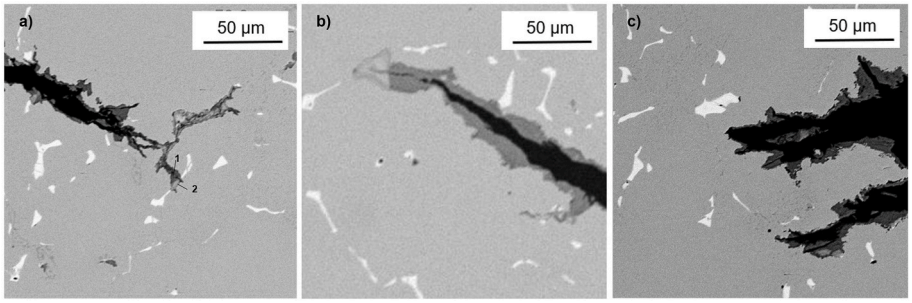

Fig. 14. SEM images of crack tips in steel A after: (a) 2100 cycles at 300–850 °C, (b) 1150 cycles at 300–950 °C, and (c) 750 cycles at 300–1000 °C.

Table 3
EDX chemical analysis (wt. %) of oxides near crack tip in steel A (points from Fig. 14a).

Point	*Cr*	*Fe*	*Nb*	*O*
1	17	15	–	67
2	19	8	30	43

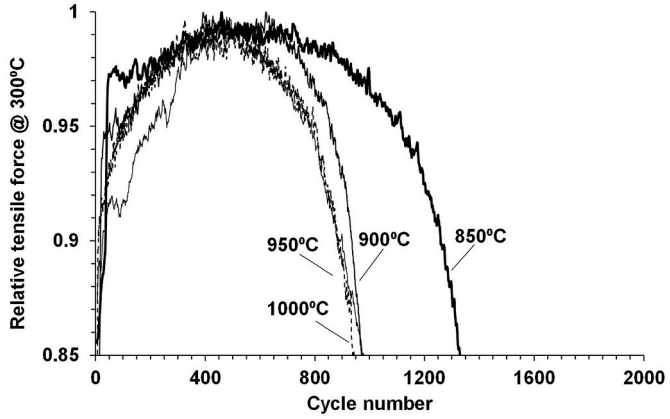

Fig. 15. Thermocycling curves of steel C applying different upper temperatures.

The results were used to determine a critical temperature for an each specific steel type and the atmospheric condition when the intensive scale spallation started to destroy the protection function of adherent *Cr*-containing oxide. This critical temperature is near 900 °C for the economical steel A, 950 °C for medium alloyed steel B, and 1000 °C for high alloyed steel C. Also, the term "extreme high temperature" could be used for temperatures above the critical temperature when the spallation mechanism is dominated in surface degradation.

However, not such positive trends with increasing *Cr/Ni* concentrations were observed in studied steels which were subjected to the transient thermo-mechanical load assisted by oxidation. Fig. 20 presents a critical number of cycles which occur before failure for each of the different upper test temperatures in three studied steels. The resilience to failure of cast *Nb*-alloyed austenitic steels during transient thermo-mechanical load did not linearly depend on *Cr/Ni* concentration for different heating cycles because of a complexity of governing mechanisms of failure for the extreme severe condition (oxidation, creep, low cycle fatigue).

It could be concluded from data presented in Fig. 20 that the optimal *Cr/Ni* level to improve the resilience of *Nb*-bearing austenitic steel depends upon the working condition. The economical steel A shows a better performance at moderate severity thermal cycling between temperatures of 300 °C–850 °C, when compared to more alloyed steels B and C. It happened because steel A had better strength/ductility combination in this cycling temperature diapason with a limited upper temperature, which was bellow a critical oxidation temperature for this steel when spallation does not occur. This indicates that the mechanical properties provided an exceptional performance of economical *Nb*-bearing 20/10 *Cr/Ni* steel A below and at near critical temperature. But increasing the upper test temperature above this critical value for steel A dramatically destroyed its performance and significantly reduced the number of cycles before failure as they dropped from 2100 to 1200. This was due to simultaneous effects of two processes: (i) intensification of oxidation assisted by scale spallation and (ii) increasing brittleness of metal matrix near tip of crack due *Cr*-carbides and possible Z-phase precipitation. To verify this assumption, a detailed TEM study were performed on the

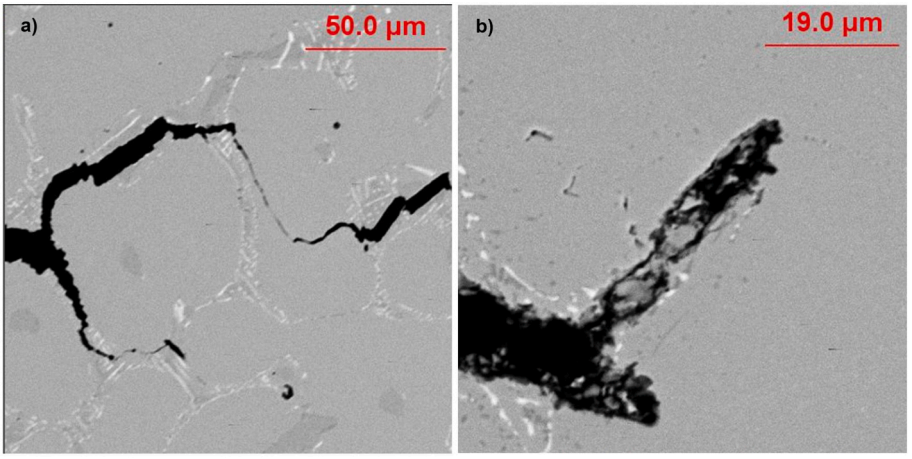

Fig. 16. SEM images of crack tips in steel C after: (a) 1055 cycles at 300–900 °C, (b) 1010 cycles at 300–1000 °C.

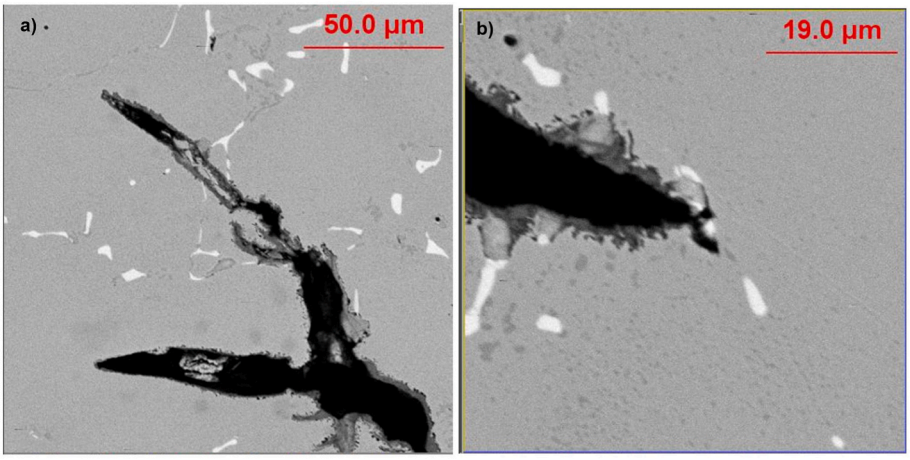

Fig. 17. SEM images of crack tips in steel B after: (a) 1830 cycles at 300–900 °C thermal-cycle, (b) 1089 cycles at 300–1000 °C thermal-cycle.

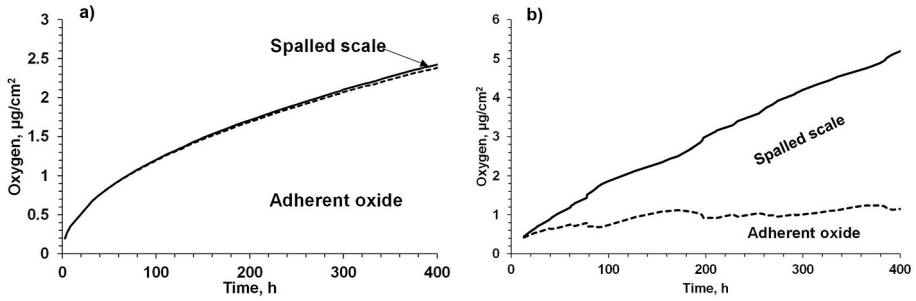

Fig. 18. Trends in oxidation kinetics assisted by scale spallation: (a) below and (n) above critical temperature.

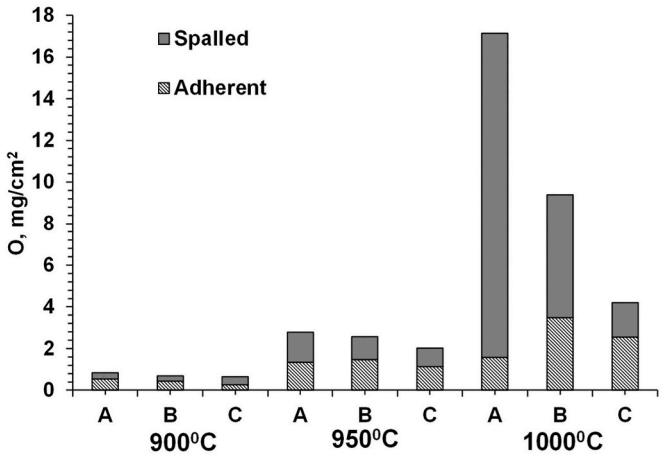

Fig. 19. Comparison of intensities of static oxidation mechanisms in Nb-bearing austenitic steels with different Cr/Ni alloying levels at different temperatures (400 h test in air).

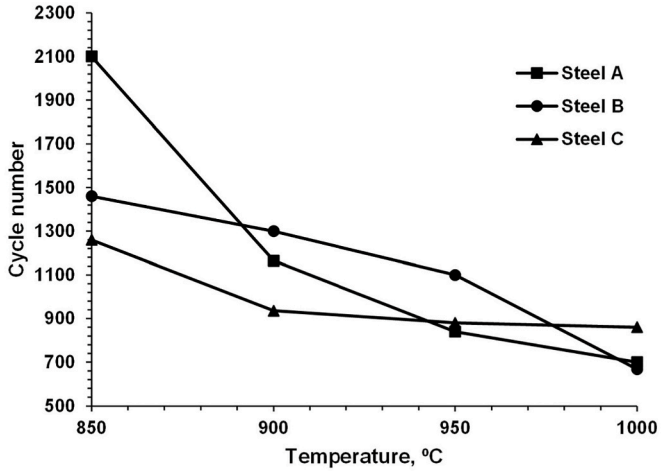

Fig. 20. Comparison of temperature effect on critical cycle number for studied steels.

thermo-cycled samples tested at 300 °C–900 °C steel A. FIB technique was used to extract foil neat tip of crack. Elemental map (Fig. 21) indicated *Cr*-depletion near crack surface due to forming *Cr*-oxide layer and cloud of small *Cr*-carbide particles in the matrix next to crack. Higher magnification image (Fig. 22) and EDX analysis (Table 4) verified compositions of the co-precipitated cubic shape *Cr*-carbide 20–50 nm particles supposed to be Z-phase, predicted from thermodynamic simulations (Fig. 2).

Medium alloyed steel B with 22/11 *Cr/Ni* has an advantage during static oxidation for 900 °C - 950 °C temperatures as compared to the economical steel A because these temperatures are just below the critical temperature for steel B, when active scale spallation can occur. In addition, high ductility after long-term annealing in this steel prevents degradation of mechanical properties during thermal cycling. All of this supports better performance of the steel B during the cycling at 900 °C - 950 °C upper temperature (Fig. 20). Finally, the resilience during the extreme thermal cycling condition tested with an upper temperature of 1000 °C, requires a combination of both high oxidation resistance and minimal softening. The excess of the material softening could promote plastic compression flow within the constrained specimen, which can

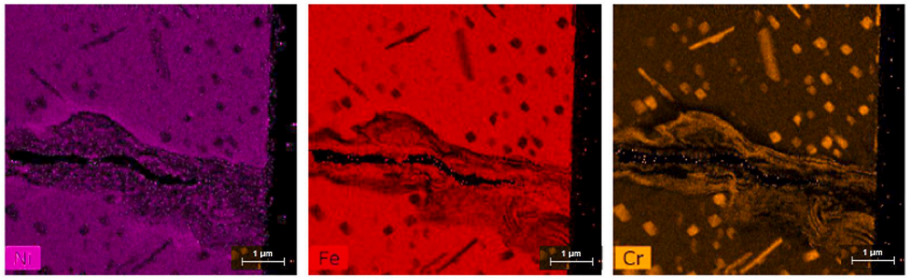

Fig. 21. TEM mapping of crack tip in thermos-cycled steel A at 300–900 °C.

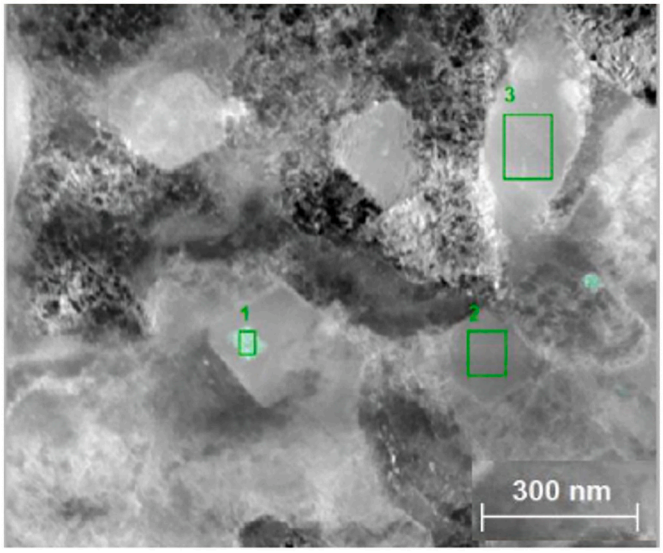

Fig. 22. Higher resolution TEM image of thermo-cycled steel A at 300–900 °C, showing co-precipitated *Cr–Nb* phase (point 1 - presumable Z-phase $Nb_{0.3}Cr_{0.3}N_{0.4}$) on *Cr*-carbide (point 2).

Table 4
EDX/TEM chemical analysis (wt. %) of precipitated phases in thermos-cycled steel A (points from Fig. 22).

Region	*Nb*	*Cr*	*Fe*	*Si*	*Ni*	*Mn*	*C*	*N*
1	36.5	42.4	11.8	0.8	2.4	1.4	–	2.2
2.3	0.6	75.6	18.9	0.2	0.8	0.9	3.0	–

generate a larger tensile stress during cooling when material will return into in the elastic region. The high alloyed steel C with 26/13 *Cr/Ni* concentrations better satisfied these requirements when compared to steels A and steel B. The study enabled us to recommend an optimal cost-effective *Cr/Ni* alloying level in *Nb*-bearing austenitic steels for different severe working conditions.

5. Conclusions

- The performance of three cast *Nb*-alloyed heat resistant austenitic steels with different *Cr/Ni* concentrations were evaluated during both static oxidation and transient thermo-mechanical loading while applying standard and custom test procedures;
- Static oxidation was performed between 900 °C and 1000 °C on air for 400 h and the critical temperatures which intensified spallation during static oxidation were determined for different *Cr/Ni* alloying levels;
- Thermal cycling of constrained specimens from each steel were tested with varying upper cycling temperatures between 850 °C and 1000 °C and resilience to failure was determined;
- SEM and TEM analyses, supported by thermodynamic simulation of the phases within the metal matrix and structure of the formed oxide layer, helped to determine the mechanisms of degradation of thermo-mechanically loaded *Cr/Ni* austenitic steels at extreme high temperatures;
- The practical recommendations for cost-effective *Cr/Ni* alloying levels for different working conditions were formulated.

Funding

This research was supported by the U.S. Department of Energy's Office of Energy Efficiency and Renewable Energy (EERE) under the Award Number DE-EE0008458.

CRediT authorship contribution statement

Simon N. Lekakh: corresponding author, Conceptualization, Methodology, Investigation. **Mario Buchely:** Methodology, Investigation. **Mei Li:** Conceptualization, Writing – review & editing. **Larry Godlewski:** Investigation, Writing – review & editing.

Declaration of competing interest

The authors declare that they have no known competing financial interests or personal relationships that could have appeared to influence the work reported in this paper.

Data availability

Data will be made available on request.

Acknowledgments

great thanks to Dr. Laura Bartlett and Dr. Ron O'Malley for supporting research, Dr. Neroslavsky for stochastic oxidation model, and Wenhui Zhu for TEM analysis.

References

[1] M. Blair, T. Stevens, Steel Castings Handbook, sixth ed., Steel Founders' Society and ASM International, Novelty, OH, USA, 1995.
[2] A. Drotlew, M. Garbiak, B. Piekarski, Cast steels for creep-resistant parts used in heat treatment plants, Arch. Foundry Eng. 12 (2012) 31.
[3] R. Voicu, et al., Creep and tensile behavior of austenitic Fe–Cr–Ni stainless steels, Mater. Sci. Eng., A 510–511 (2009) 185.
[4] M.P. De Oliveira, et al., Recent developments in niobium containing austenitic stainless steels for thermal power plants, in: Energy Materials, Springer, Cham, 2014, https://doi.org/10.1007/978-3-319-48765-6_30.
[5] T. Okuyama, et al., Effect of Nb on thermal-shock resistance of austenitic heat resistant cast steel, Mater. Transact., Japan Inst. Metals Mater. 9 (61) (2020) 1711.
[6] A. Carreon et al., Development of a Novel Heat-resistant Austenitic Cast Steel with Improved Thermal Fatigue Resistance, Int. J. Metalcast., Published online 06.1022, https://doi.org/10.1007/s40962-022-00838-1.

[7] Y. Zhang, et al., Creep behavior at 1273 K in Nb-bearing austenitic heat-resistant cast steels developed for exhaust component applications, *Metall. Mater. Trans.* A 47 (2016) 3289.
[8] H. Zhao, et al., The Effect of metal-carbide morphology on the thermomechanical fatigue (TMF) behavior of cast austenitic alloys for exhaust manifolds, Procedia Eng. 133 (2015) 669.
[9] H. Zhao, et al., Mechanical response and dislocation substructure of a cast austenitic steel under low cycle fatigue at elevated temperatures, Mater. Sci. Eng., A 703 (2017) 422.
[10] S. Huang, et al., Effect of niobium addition on the high-temperature oxidation behavior of 22Cr25NiWCoCu stainless steel in air, Metals 9 (2019) 975.
[11] D. Dulieu, The role of niobium in austenitic and duplex stainless steels, in: International Symposium Niobium, 2001. https://niobium.tech/-/media/NiobiumTech/Attachments-Biblioteca-Tecnica/NT_The-role-of-niobium-in-austenitic-and-duplex-stainless-steels.pdf.
[12] S. Lekakh, et al., Effect of spallation on oxidation kinetics of heat-resistant Cr–Ni austenitic steels on air and combustion atmosphere, High Temp. Corros. Mater. 99 (2023) 79.
[13] S.N. Lekakh, et al., Stochastic model for high temperature oxidation of Cr-Ni austenitic steels assisted by spallation, Oxid. Metals 98 (2022) 239.
[14] S. Lekakh, et al., Thermo-cycling fatigue of SiMo ductile iron using a novel thermo-mechanical test, Int. J. Fatig. 148 (2021), 106218.